TRENDS IN SCIENCES 2025; 22(6): 9762 RESEARCH ARTICLE
https://doi.org/10.48048/tis.2025.9762

Fabrication of Antibiofilm-Based-Polymer Nanocomposite for Biophysical Applications

Rawaa A. Abdul-Nabi[1,2] and Ehssan Al-Bermany[2,*]

[1]*Department of Electrical Engineering Techniques, Al-Mussaib Technical College, Al-Furat AL-Awssat Technical University, Najaf Governorate, Iraq*
[2]*Department of Physics, College of Education for Pure Sciences, University of Babylon, Babylon Governorate, Iraq*

([*]Corresponding author's e-mail: ehssan@uobabylon.edu.iq)

Received: 12 January 2025, Revised: 19 February 2025, Accepted: 26 February 2025, Published: 1 May 2025

Abstract

Polymer nanocomposites attracted significant interest because of their effective characterization and low cost. This investigation aims to fabricate newly cost-effective blended polymer polyethylene oxide (PEO), carboxymethyl cellulose (CMC), and conductive nano-polyaniline (PANI) were improved by different loading ratios of hybrid graphene oxide (Fixed ratio = 0.05 %) and different loading ratio of silicon nitride (0.05, 0.25, and 0.45 %), (GO-Si_3N_4) nanomaterials to fabricated nanocomposites. PEO-CMC-PANI/GO-Si_3N_4 composites were fabricated using the acoustic-ultrasonic method. The semicrystalline performance of samples was proved using X-ray diffraction, and Fourier-transform infrared spectroscopy exposed strong interfacial interaction. Field emission scanning electron microscopies showed homogenous samples with fine nanomaterial dispersion in the matrix, revealing significant changes. The transparency of the samples was increased with the rise in the nanomaterial's ratio, with the main electron transitions at about 280 nm wavelengths due to reducing the optical band gap from 3.5 to 2.6 and 2.8 eV of allowed and forbidden transitions. The inhibition of biofilm formation by the nanocomposite at a concentration of 5 % for bacterial isolates of *Escherichia coli* and *Streptococcus mutans* was increased compared to untreated bacteria. The optical density of *S. mutants* and *E. coli* was improved from 0.95, 0.2, and 0.4 mm, respectively. These nanocomposites presented good and cheap materials with a high aptitude for killing bacteria. They could be used in various biological and related applications, such as coating operating rooms, tools, cleaning, and even replacing traditional disinfectants.

Keywords: Polymer, Silicon, Graphene, Biofilm, *Escherichia coli*, *Streptococcus mutans*

Introduction

An important field of research is the investigation of the optical properties of antibacterial materials for several probable reasons, including the following [1]: The presence and activity of antibacterial agents can be detected and monitored with the help of optical characteristics, which can be utilized for both detection and monitoring purposes [2]. Researchers can build optical sensing techniques to identify the presence of bacteria or evaluate the efficacy of antibacterial treatments by analyzing the interaction of light with antibacterial materials [3]. This allows the researchers to develop strategies using light. This is especially helpful in hospital settings, where it is necessary to guarantee that sufficient cleanliness and sterilization are maintained [4,5].

Understanding the mechanism of action of antibacterial materials is possible by 1st understanding their optical features [6]. For instance, if a substance demonstrates particular optical qualities when it comes into contact with bacteria, it can indicate that specific chemical or physical processes are taking place that contribute to the material's antibacterial activity [7]. By examining these characteristics, researchers can acquire a more comprehensive comprehension of the functioning of antibacterial materials and potentially

enhance their efficiency [8]. The surface characteristics of antibacterial materials can impact the material's optical properties. Researchers can explore the optical response of modified surfaces to bacteria or bacterial byproducts to produce surfaces that are either naturally antibacterial or activated when bacteria come into contact [9,10].

Antibiotics are a significant breakthrough in the field of treatment, playing a vital role in saving many lives by rendering formerly fatal illnesses treatable [11]. The dependability of antibiotics is the cornerstone of modern medicine and has enabled the advancement of various medical operations that were before unattainable. Every facet of modern medicine encompasses surgical interventions and therapies for burns and injuries. The discovery of antimicrobial medications made all of this possible [12]. However, scholars and healthcare professionals need help identifying a resolution to the escalating issue of antibiotic resistance, which is especially prevalent in healthcare environments. Immediate action must be taken to resolve this issue as it threatens the fundamental principles on which modern medicine was founded [13]. Bacteria acquire resistance to antibacterial treatments in several ways, necessitating a novel approach to produce new bactericidal agents. The quest for novel antimicrobial drugs or enhancements in the efficacy of existing ones is imperative [14].

Nanomaterials can be considered based on their dimensions: 0, 1, 2, and 3-dimensional thin films and layers [15]. Studies have demonstrated significant interest in inorganic nanoparticles due to their potential for various uses, such as their antibacterial properties [16]. Graphene oxide (GO) has shown promising potential as both an antibacterial agent and an antibiotic carrier due to several mechanisms [17]. It uses a physical damage procedure using the sharp edges of their nanosheets that can penetrate and disrupt bacterial cell membranes, leading to cell death. The addition strategy of GO is oxidative stress, where it can generate reactive oxygen species (ROS) that are the bases of oxidative stress in bacterial cells, lipids, DNA, and damaging proteins. Moreover, photothermal effects as light irradiation by GO, can convert light energy into heat, enhancing its antibacterial activity by causing thermal damage to bacterial cells [18]. Studies have demonstrated that GO can effectively inhibit the growth of various bacteria, including *E. coli* and *S. aureus* [19]. GO can coat medical devices, reducing the risk of bacterial infections. Incorporating GO into wound dressings can prevent bacterial infections and promote healing [18]. The large surface area of GO is associated with controlling the release of antibiotics and carrying enormous quantities of antibiotics essential for effective concentrations to be maintained for an extended duration [20]. GO can be combined with different antibiotics, doxycycline and ciprofloxacin, which improve the effectiveness against bacteria due to the GO stability compared to antibiotics alone [18], and ensure its safety and efficacy in medical applications [21]. In addition, GO-based sensors can detect cancer biomarkers at deficient concentrations, aiding in early diagnosis [22].

Another interesting nanomaterial is silicon nitride (Si_3N_4), a ceramic material known for its exceptional mechanical properties, chemical stability, and biocompatibility [23]. Although its main applications are in bearings, cutting tools, and implants, research has also investigated its potential in medicinal fields, such as antibacterial, antibiotic administration, and anticancer therapy [24]. The rough surface shape of Si_3N_4 at the micro- and nanoscale prevents bacterial adherence and growth by disrupting bacterial cell walls. Si_3N_4 exhibits chemical inertness, which enhances its ability to resist bacterial colonization and the production of biofilms. By introducing additional elements, Si_3N_4 can be doped to improve its antibacterial capabilities by releasing antimicrobial ions [25]. Si_3N_4 is employed in orthopedic and dental implants because of its antibacterial qualities. Also, it can reduce the probability of infection during surgical procedures. That makes Si_3N_4 a nondonated material for coating medical devices that can efficiently inhibit bacterial infections [24]. Si_3N_4 exhibits an outstanding biocompatibility that is suitable for drug delivery systems. Si_3N_4 can be controlled to release antibiotics at a regulated rate, and therapeutic doses are maintained for extended periods. The antibiotic is guaranteed not to degrade because of the chemical stability of Si_3N_4 [26]. It is a practical material for delivering the drag of anticancer through the porosity and high surface area that gives it features for loading and control, realizing the therapeutic chemicals. It is also presented as an efficient composite for treating bone infections and other localized illnesses by

deliberately discharging antibiotics [27]. PEO can dissolve in many substances and has a large molecular weight [28]. PEO is compatible with various applications. For instance, PEO is used in drug delivery, the environment, medicine, industry, etc. [29]. CMC can dissolve in water, is semicrystalline, is low-cost, and has low conductivity and strength. Also, it is compatible and non-toxic and is used in applications such as cosmetics, living organisms, industrial, pharmaceutical, food, etc. [30]. PANI has high electrical conductivity and thermal stability, lower density than metals, a significant visible light absorption ability, good energy storage capabilities, and low cost. Amazing PANI characterizations are used it in various applications, such as drug delivery, display devices, photovoltaic cells, plastic batteries, etc. [31]. This study focused on the impact of nanomaterials on improving nanocomposites as effective and low-cost antibacterial materials could replace traditional use.

Materials and methods

The details, molecular weight, chemical form, and supplier company of materials used in this study are shown in **Table 1**. PEO with MW, 100,000 g mol^{-1} provided by Sigma-Aldrich Company, UK. CMC with MW, 700,000 g mol^{-1} supplied by Cheng Du Micxy Chemical Co., Ltd., China. Polyaniline is a conductive polymer with nanoparticles (20 nm)-dark/light green-black, with MW 150,000 g mol^{-1}, manufactured by Panichem. Co., LTD, Korea. Silicon Nitride nanopowders with size (15 - 30 nm) and grey white and MW, 140.28 g mol^{-1}. Full characterization of the synthesized GO was provided in the publication [21].

Solution-sonication-casting methods were developed and used to prepare the samples following the procedures: First, all the polymer was dissolved in distilled water (DW) at a ratio of 5 g/100 mL independently.

Secondly, after dissolving each polymer, it was mixed for 24 h to prepare the blended polymers at a ratio of (60:30:10 %) of (PEO: CMC: PANI) at room temperature (RT) (25 ± 3 °C) for 24 h to achieve optimal dissolution and homogeneity.

Thirdly, the nanomaterial was separately dispersed in deionized water using a stirrer with 100 mg/100 mL, followed by 10 min of bath sonication for every hour of mixing to achieve optimal dispersion.

Fourthly, to achieve the best possible results of the novel quinary nanocomposites. Nanomaterials were mixed with different concentrations (1, 3, and 5 %) of (GO: Si_3N_4) with a fixed concentration of GO and various concentrations of Si_3N_4, together with the assistance of sonication for 30 minutes.

Fifthly, combined nanomaterials were loaded in blend polymers for 7 days using a stirrer and 30 minutes of sonication in a bath.

Finally, samples were stored in class-celled pots for the biofilm test, and others were dried on a glass slide for XRD and FESEM and utilized as solutions for other tests. The thickness of the samples was 60 microns.

Table 1 The ratios of micing sample components.

Samples ID	Concentration, %				Drying
	PEO_{100K}	CMC	PANI	GO + Si_3N_4	
Blend polymers: B	60	30	10	-	In the oven at 50 °C for XRD and FESEM
Composite 1: N1 %	60	30	9.9	0.05:0.05	
Composite 2: N3 %	60	30	7	0.05:0.25	
Composite 3: N5 %	60	30	5	0.05:0.45	

Results and discussion

Figure 1 presents the XRD patterns for the pure (CMC/PANI/PEO) blend sample and its nanocomposites filled with the mixture of GO + Si_3N_4 nanoparticles at different ratios (1, 3, and 5 %). The XRD was set up to run 28 times for 30 min for each XRD test for reliable results. Because the PEO polymer has a semi-crystalline structure, the XRD pattern of ternary blended polymers (B) showed that the polymer matrix is semi-crystalline. Where PEO is associated with the primary peaks at 18.4 and 22.7 °. PANI showed additional tiny peaks, whereas the CMC semi-crystalline peak, seen at 22.3 °, overlapped with PEO peaks. The peaks of nanocomposites revealed a minor

movement in the locations of most of the peaks from their initial positions. The contribution of (GO + Si_3N_4) nanomaterials at various ratios resulted in the shifting of most peaks with increased peak intensity and nanomaterial loading ratios in the matrix.

The XRD patterns of the blend filled with the contribution of (GO-Si_3N_4) nanomaterials at different ratios (1, 3, and 5 wt.%) revealed a reduction of the peak intensity with the addition and raising of the (Si_3N_4) nanoparticles ratio. Moreover, the peaks revealed a slight shifting in most of the peaks from their original positions. Specifically, NC1 revealed a sign of GO in 11.1 and 40.02 ° [32], and all other XRD diffraction peaks might be indexed to the Si_3N_4, a hexagonal structure matched (JCPDS Card no. 41-0360), and other reports [33]. In addition, the obtained XRD results proved the strong interaction and good distribution of the (GO-Si_3N_4) nanoparticles and the matrix blend, as demonstrated by FT-IR results and literature [34,35]. Most peaks were shifted, and the intensity at around 19 ° increased to become higher compared with other peaks and blended samples; moreover, the dissolution of (GO-Si_3N_4) nanoparticles within the structure of the PEO-CMC-PANI polymer blend.

X-ray diffraction determines any material's structural factors, which are crucial in explaining many of the material's physical properties. When X-ray light of wavelength (λ) is projected at a Bragg diffraction angle (θ) onto a crystal lattice, the incoming X-rays interact constructively with the sample if the circumstances meet Bragg's law, as shown in **Figure 1** [36].

$$2d \sin\Theta = n\lambda \quad (1)$$

where (d) means distance and (n) is diffraction rating.

The crystal size (D) in nm units was considered using the Scherrer Eq. (2) [37].

$$D = k\lambda/\beta\cos(\theta) \quad (2)$$

(D) means the size of the crystal (k = 0.9), and (β) means the complete breadth at half the highest point (FWHM).

In **Table 1**, calculations showed that the crystalline size of samples loaded with NPs increased significantly after increasing the loading of GO-Si_3N_4 by 16.71, 19.5, and 20.2, then reduced to 17.2 nm for B, NC1, NC2, and NC3, respectively. At the same time, the samples had an increase in lattice strain of up to 8.58, 6.77, and 8.80 % for NC1, NC2, and NC3, respectively.

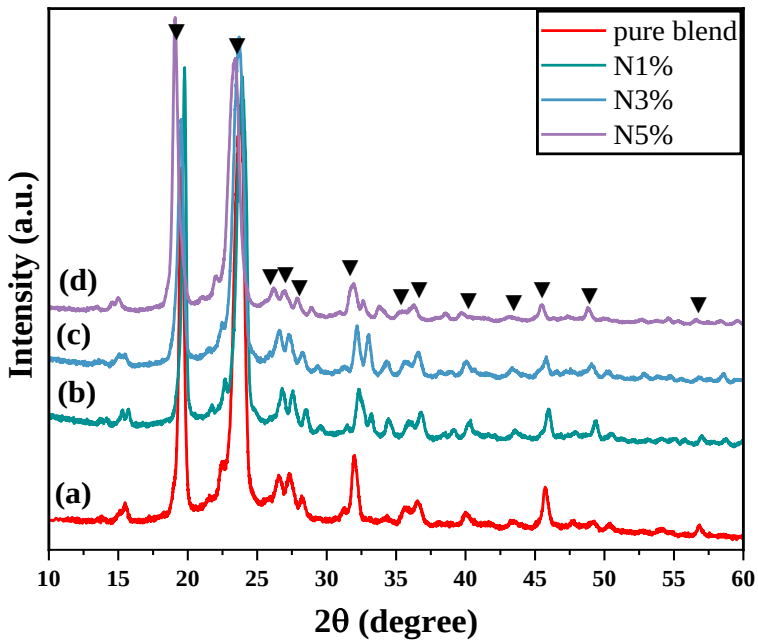

Figure 1 XRD patterns of (a) B, (b) N1 %, (c) N3 %, and (d) N5 %.

Table 1 provides an overview of the diffraction angle (2θ), FWHM (β), d-spacing, average crystallite size, and size of the crystallites for both blended polymers and samples loaded with different amounts of GO-Si_3N_4.

Samples	2θ (°)	d (nm)	β (°)	D (nm)	Average crystallite size (nm)
B	14.3	6.206	0.699	11.954	16.711
	18.4	4.805	0.423	19.826	
	22.7	3.898	0.493	17.149	
	25.4	3.497	0.740	11.485	
	26.2	3.388	0.604	14.099	
	30.8	2.891	0.490	17.550	
	35.5	2.695	0.612	14.214	
	38.8	2.309	0.595	14.757	
	44.7	2.131	0.418	21.428	
	55.8	2.028	0.380	24.652	
NC1	15.3	5.72128	0.3958	21.144	19.509
	18.4	4.55316	0.2336	35.968	
	19.5	4.12579	1.3468	26.947	
	23.7	3.749	0.3189	26.575	
	26.6	3.353	0.720	11.832	
	27.5	3.259	0.422	20.201	
	32	2.779	0.458	18.823	
	33	2.713	0.406	21.296	
	34.3	2.612	0.405	21.390	
	35.5	2.510	0.649	13.400	
	36.5	2.456	0.492	17.726	
	40.2	2.355	0.622	14.190	
	45.9	2.317	0.584	15.399	
NC2	15.3	5.79642	0.3665	22.834	20.266
	19.7	5.63067	0.317	26.556	
	23.8	3.72757	0.3918	21.634	
	26.6	3.68515	0.6201	13.744	
	27.5	3.23225	0.3937	21.689	
	32	3.12918	0.6002	14.376	
	33	3.02161	0.3234	26.748	
	34.3	2.6	0.3744	23.184	
	35.9	2.49265	0.6366	13.695	
	36.8	2.44235	0.4491	19.463	
	40.2	2.23773	0.4649	18.998	
	46	2.073	0.2705	33.310	

Samples	2θ (°)	d (nm)	β (°)	D (nm)	Average crystallite size (nm)
	49.3	1.97412	0.3854	23.679	
NC3	15	5.8968	0.434	19.276	17.294
	19.7	4.64319	0.3972	21.194	
	23.4	4.53694	0.7952	10.652	
	26.3	3.40491	0.9785	8.705	
	27	3.29871	0.3937	21.666	
	32	3.19534	0.4074	21.179	
	32.6	3.08384	0.4033	21.427	
	33	2.6447	0.534	16.233	
	36.8	2.52849	0.5514	15.852	
	40.2	2.26348	0.6432	13.731	
	45.5	2.19758	0.4427	20.316	
	49.3	1.86393	0.3854	23.679	

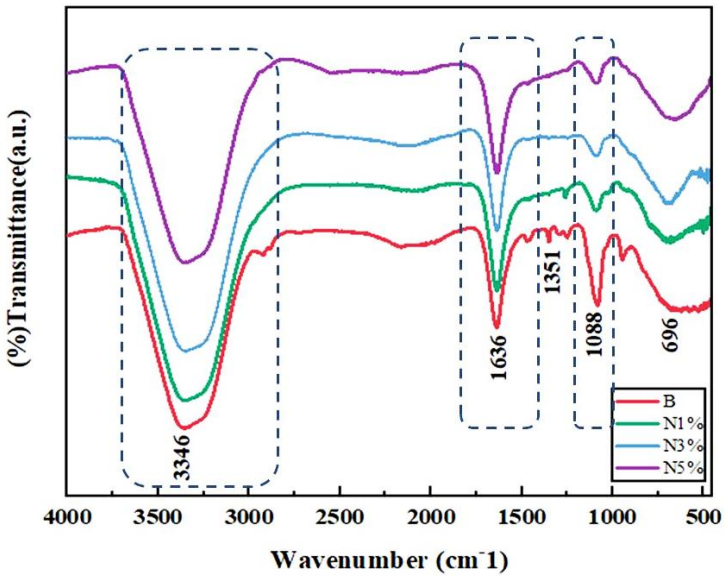

Figure 2 FTIR spectrum for blend polymers and their nanocomposites.

Figure 2 displays the doping of (GO-Si_3N_4) nanoparticles in the blended (PEO-CMC-PANI) polymers. Several major results are presented in the FTIR spectrum of the pristine blended polymer and (PEO-CMC-PANI/GO-Si_3N_4) nanocomposites. The FTIR spectrum was set up to run 16 times in each FTIR run, and the sample was run for reliable results. The most functional peaks of the spectrum of blended polymer and quinary (N1, N3, and N5 %) nanocomposites match peaks in the contained polymers peaks spectrum. In general, samples exposed strong O-H peaks at 3,346 and 1,636 cm^{-1}. The nanomaterial contribution in nanocomposites looked to be responsible for presenting the C-O-C bond and helped to form a complex network between the oxygen functional groups of GO-Si_3N_4 nanomaterial and blended polymers, which strongly agrees with other findings [38].

All samples generally showed strong absorption peaks at 3,346, 1,636, 1,088, and 696 cm^{-1}, as hydrogen interactions between the ternary blended polymer (B) and nanomaterials. The contribution of the binary nanomaterial in nanocomposites appeared, which is responsible for the decrease in the intensity of most peaks. This is connected with creating the network

among GO and Si_3N_4 nonmaterial and polymers, which strongly agrees with other findings [38]. Structural features of the blended polymer were not affected after the fabrication of the nanocomposites in agreement with another report [39]. **Table 3** displays the functional group and corresponding FTIR peaks.

Table 3 The functional group and corresponding FTIR peaks.

FTIR Peak (cm^{-1})	Functional group	References
3,346	O-H stretching (CMC) and/or stretch vibration N-JH (PANI)	[40,41]
2,890	C-H starching in CMC	[42]
1,636	C=C quinoid ring stretching (N=Q=N) in PANI structure/(–COO-) asymmetric vibrations group generated from (–COO-Na+) Structure/NH2 bending	[42,46]
1,351	bending C-H peak of PEO, stretching C-O and C=C stretching of the benzene ring,	[41,42]
1,088	stretching C-O-C vibration	[47,48]
1,258	asymmetric CH_2-twisting/ C-N stretching of the secondary aromatic ring	[49,50]
948	C-H rocking vibration of a methylene group,	[51]
696	presence of iron oxide	[51,53]

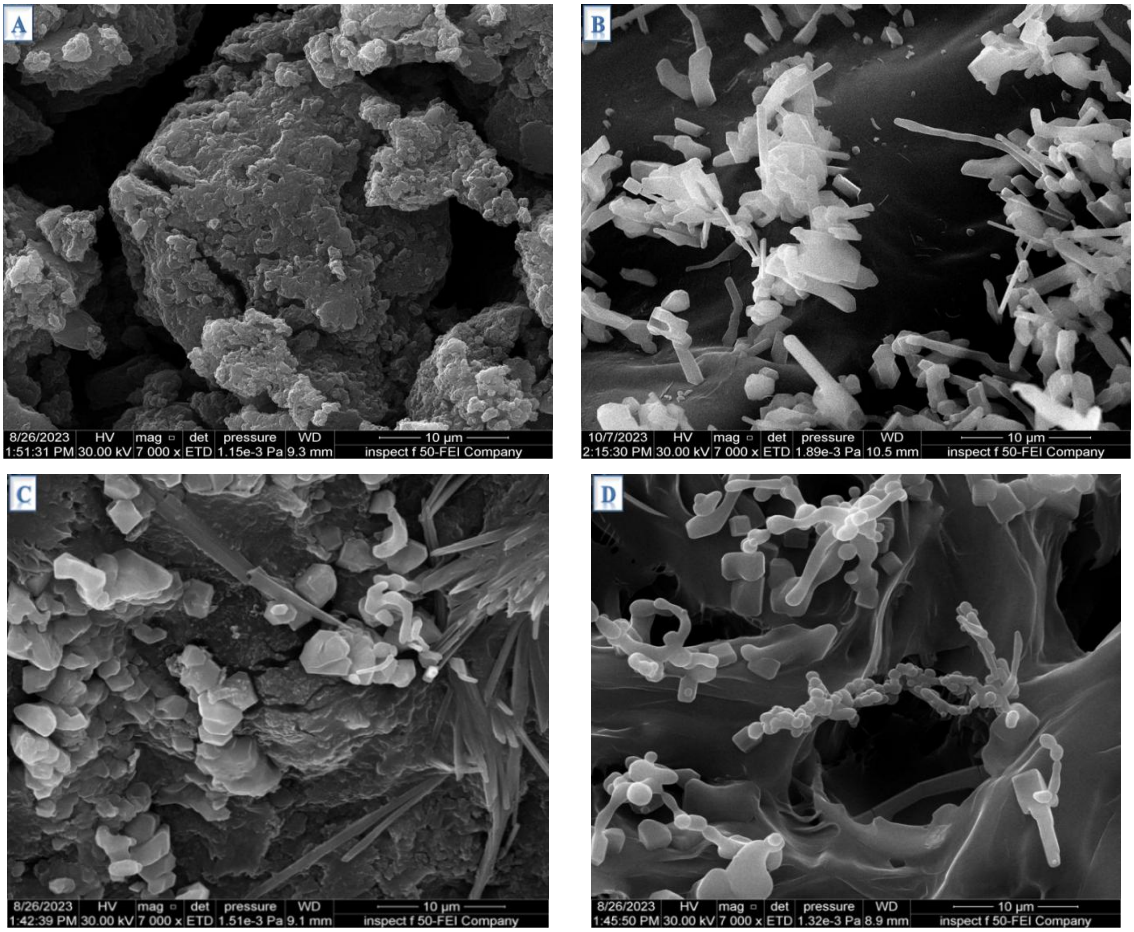

Figure 3 FESEM images of (A) B, (B) N1 %, (C) N3 %, and (D) N5 %.

When the polymers are mixed, the sample of blended polymer B shows a significant surface change, as shown in **Figure 3(A)**. It presents a rough, uneven, granular appearance with some agglomerations and particles of different sizes and a cauliflower-like structure with deep cavities. When nanomaterials were

loaded at 1 % to the blended polymer mixture, the bonding between the polymers improved and became uniformly distributed, the surface became smoother with the attached nanomaterials, the granular shape was lost, and the deep cavities and some tangled threads appeared for a similar network of PEO, CMC, PANI, and nanomaterials. When nanomaterials were loaded at 1 % into the polymer mixture **Figure 3(B)**, the bonding between the polymers improved and became uniformly distributed. The surface became smoother with the attached nanomaterials. The granular shape was lost, and the deep cavities and some tangled threads appeared for a similar PEO, CMC, PANI, and nanomaterials network. Increasing the Si_3N_4 ratio in the sample to 3 %, as shown in **Figure 3(C)**, helped provide a porous structure resulting from PANI nanoparticles and nanofibers with complex network shapes where polymers are linked together in an arm-like manner, interspersed with some pores as well as particles of various clusters. The sharp edges of the graphene oxide layers were also revealed. In **Figure 3(D)**, increasing the nanomaterials to 5 % increased the width of the porous structure resulting from the nanoparticles and nanofibers of PANI; in addition, the surface became smoother in other parts, although its increased value was modest compared to the blended sample [54].

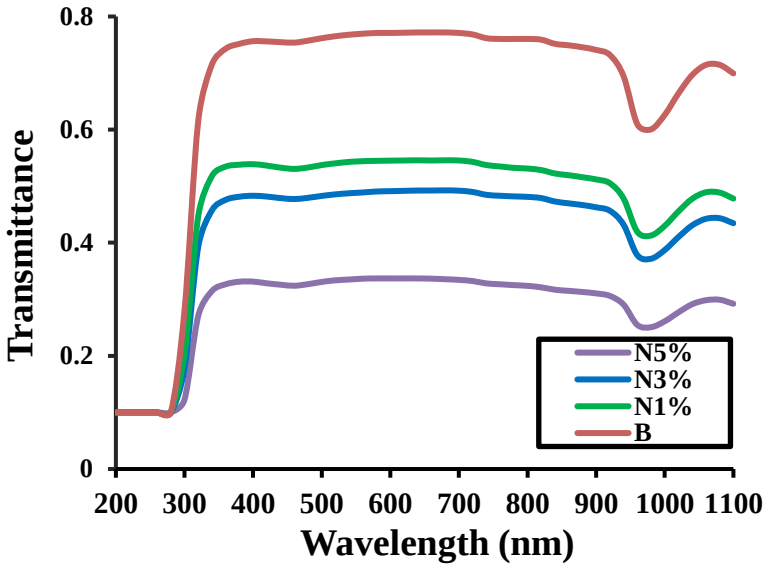

Figure 4 Transmittance of samples with wavelength.

The change in the transmittance spectrum as a function of the wavelength of the pure mixed polymer and the compound loaded with different percentages (1, 3, and 5 %) of the binary nanomaterial GO-Si_3N_4 appears in **Figure 4**. The UV-Vis spectrum was set up to run 5 times for each sample, and the average was taken for reliable results. The transmittance was the lowest possible at the basic absorption edge (short wavelengths). The transmittance increased with increasing wavelength, showing a sudden and strong increase until it stabilizes after the wavelength (340 nm). On the other hand, the greatest value of transmittance was in the near-infrared and visible rays (0.77) and then gradually decreased with an increase in the percentage of GO-Si_3N_4, as loading the binary material GO-Si_3N_4 led to the accumulation of NPs, which increased the surface roughness, and thus the light surface fragmentation increases with increasing loading rates, which causes a decreased permeability. The optical energy gap values of the indirect transition were calculated according to Tauc's relation [55].

$$\alpha h\nu = B\,(h\nu - E_g)^r \quad (3)$$

The values of r = 2 and 3 for permitted and forbidden indirect transitions, while (B), (h), and (E_g) represent constants, photon energy, and the energy gap, respectively.

Results are revealed in **Table 4** and **Figure 5**. The obtained result matches the same behavior of the literature that used $NiCl_2 \cdot 6H_2O$ in (PVDF-PHFP). The nanofiber had an optical bandgap reduced from 3.24 to

3.10 eV [56]. These highly transparent samples in this wide wavenumber range could open a wide way for various optical applications such as optical sensors, solar cells, etc.

Table 4 The optical energy gap values of the indirect transition in eV for samples.

Sample	Allowed	Forbidden
B	3.5	3.5
N1 %	3.2	3.3
N3 %	2.9	3.1
N5 %	2.6	2.8

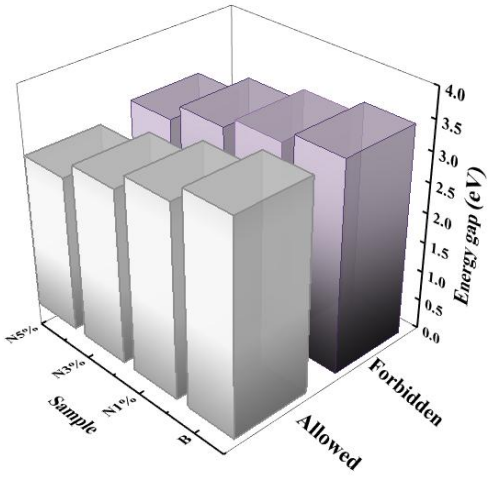

Figure 5 Depict the allowed and forbidden optical energy gap for the B, N1, N3, and N5 %.

Antibiofilm activity

Biofilm is one of the characteristics of virulence that can be formed by gram-negative and gram-positive bacteria, regardless of whether they are isolated from the body or from outside the body. This is especially true for bacteria that are found on medical devices such as catheters and dialysis devices, as well as in burns, industrial water, and other surfaces of organic and inorganic materials [57]. There are 4 stages to the life cycle of a microbial biofilm as shown in **Figure 6(A)** [58].

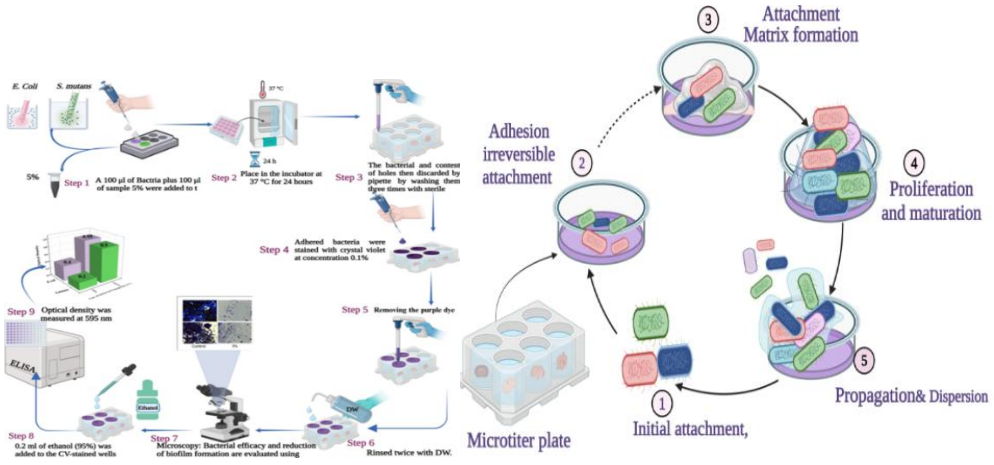

(A) (B)

Figure 6 Schematic diagrams of (A) the different steps of Biofilm formation and (B) evaluation of the antibiofilm activity of the Nanoantigen.

The procedure was performed using a sterile 96-hole microtiter plate assay method (Crystal violet staining), as shown in **Figure 6(B)**. According to the literature, individuals with urinary tract infections brought on by *E. coli* bacteria that form biofilms are more likely to contract the illness again after recovering. The study examined how the crystal violet color compound attaches to adherent cells. The studied bacterial isolates were able to produce biofilms. The results of the CV test revealed that 0.1 % that the tested bacterial isolates could form biofilms, and 100 % for *E. coli* and *Streptococcus.* Studies showed that people with urinary tract infections caused by biofilm-producing *E. coli* bacteria are more susceptible to re-infection with the disease after recovery from it [59,60]. In addition, treatment with (100 microliters) of Si_3N_4-GO NPs results in rapid biofilm removal. The samples were run 3 times to confirm the obtained results, and the standard deviation was ± 0.02. **Figures 7(A) - 7(C)** depict the results of *E. coli* and *S. mutans* isolates treated with GO-Si_3N_4. The 5 % nanocomposite inhibits biofilm formation (-) with a value of 0.2 and 0.4 for *S. mutans* and *E. coli* bacteria, respectively. In addition, there is an inverse correlation between the optical density and the addition of the nanomaterial, as a decrease in the optical density is noticed with the treatment of bacteria with the nanomaterial.

This demonstrates the ability of GO to penetrate the EPS of biofilms and destroy their 3-dimensional structure, as shown in **Figure 7(C)**. It prevents the formation of biofilms either by preventing the synthesis of exogenous sugars, which is considered an important step in the formation of biofilms by entering the aquaporin channels that carry water and nutrients through the layers of sugars present on the bacterial cell wall, or the formation of biofilms is reduced by another behavior, which is intervention. All produced biofilms were detached from the wells, in the proteins and enzymes necessary for adhesion and entry into the bacterial cell. As shown in **Table 5**. It was found that the rate of optical density of *S. mutans* was better than that of *E. coli.* This indicates more bacterial inhibition, consistent with the literature [61-64]. The samples were run 3 times to confirm the obtained results, and the standard deviation was ± 0.02.

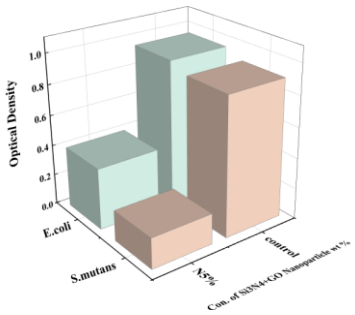

(A)

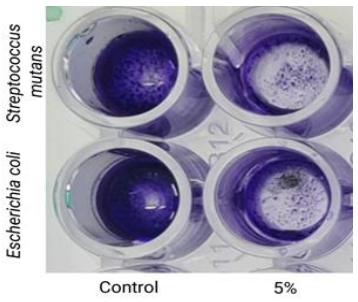

(B)

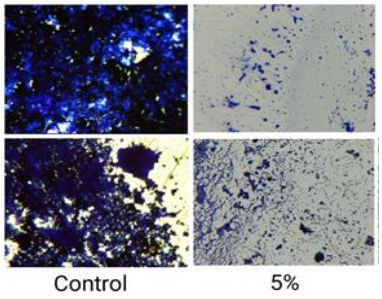

(C)

Figure 7 (A) Antibiofilm (optical density) of isolates of *S. mutans* compared to *E. coli* of control (without bacteria) and N5 % sample, (B) image of *E. coli* and *S. mutans* bacteria adhered with crystal violet in a microtiter plate, of 5 % GO-Si_3N_4 concentration compared to control (without bacteria) and (C) image of *E. coli* and *S. mutans* after adhered bacteria stained with crystal violet by microscopy.

Table 5 The optical density of nano-fabricated antibiofilm.

Sample	Optical density (mm)	
	S. mutans	***E. coli***
Control	0.9	0.95
N5 %	0.2	0.4

Conclusions

Effective and low-cost new polymer nanocomposites were successfully fabricated. The samples showed significant interaction between their components, and the addition of nanomaterials increased this interaction without affecting the main structure. Samples showed reduced transmittance, optical band gap, and significantly increased electron transitions that helped enhance the inhibition in biofilm formation, increasing with increasing concentrations for the 2 bacterial isolates. The promising nanocomposite exhibited excellent optical and antibacterial characteristics that can be employed in optical devices, filters, and antimicrobials.

Acknowledgments

RA Abdul-Nabi did the investigation, methodology, 1st analysis, and wrote the 1st draft. E Al-Bermany is responsible for project administration, suggestions, investigation, review, and editing of the final manuscript.

References

[1] C McGoverin, C Steed, A Esan, J Robertson, S Swift and F Vanholsbeeck. Optical methods for bacterial detection and characterization. *APL Photonics* 2021; **6**, 80903.

[2] AI Alawi, E Al-Bermany, RS Alnayli, MM Sabri, NM Ahmed and AKJ Albermany. Impact of SiO_2-GO hybrid nanomaterials on opto-electronic behavior for novel glass quinary (PAAm-PVP-PVA/SiO_2-GO) hybrid nanocomposite for antibacterial activity and shielding applications. *Optical and Quantum Electronics* 2024; **56**, 429.

[3] N Idil, S Aslıyüce, I Perçin and B Mattiasson. Recent advances in optical sensing for the detection of microbial contaminants. *Micromachines* 2023; **14(9)**, 1668.

[4] AM Upadhyaya, MK Hasan, S Abdel-Khalek, R Hassan, MC Srivastava, P Sharan, S Islam, AME Saad and N Vo. A comprehensive review of the optical micro-electromechanical sensors for the biomedical application. *Frontiers in Public Health* 2021; **9**, 759032.

[5] AKJ Rashid, ED Jawad and BY Kadem. A study of some mechanical properties of iraqi palm fiber-PVA composite by ultrasonic. *European Journal of Scientific Research* 2011; **61(2)**, 203-209.

[6] MA Salam, FH Alsultany, E Al-Bermany, MM Sabri, K Abdali and NM Ahmed. Impact of graphene oxide nanosheets and polymethyl methacrylate on nano/hybrid-based restoration dental filler composites: Ultrasound behavior and antibacterial activity. *Journal of Ultrasound* 2024. https://doi.org/10.1007/s40477-023-00855-8

[7] J Sahoo, S Sarkhel, N Mukherjee and A Jaiswal. Nanomaterial-based antimicrobial coating for biomedical implants: New age solution for biofilm-associated infections. *ACS Omega* 2022; **7(50)**, 45962-45980.

[8] SM Imani, L Ladouceur, T Marshall, R Maclachlan, L Soleymani and TF Didar. Antimicrobial nanomaterials and coatings: Current mechanisms and future perspectives to control the spread of viruses including SARS-CoV-2. *ACS Nano* 2020; **14(10)**, 12341-12369.

[9] EO Ogunsona, R Muthuraj, E Ojogbo, O Valerio and TH Mekonnen. Engineered nanomaterials for antimicrobial applications: A review. *Applied Materials Today* 2020; **18**, 100473.

[10] RA Ghazi, KH Al-Mayalee, E Al-Bermany, FS Hashim and AKJ Albermany. Impact of polymer molecular weights and graphene nanosheets on fabricated PVA-PEG/GO nanocomposites: Morphology, sorption behavior and shielding application. *AIMS Materials Science* 2022; **9(4)**, 584-603.

[11] TM Uddin, AJ Chakraborty, A Khusro, BRM

Zidan, S Mitra, TB Emran, K Dhama, MKH Ripon, M Gajdács, MUK Sahibzada, MJ Hossain and N Koirala. Antibiotic resistance in microbes: History, mechanisms, therapeutic strategies and future prospects. *Journal of Infection and Public Health* 2021; **14(12)**, 1750-1766.

[12] RAK Al-Refai'a, K Abdali and E Al-Bermany. Some chloroquine derivatives for promising new antifungal drugs and absorption behavior. *International Journal of Nanoscience* 2024; **23(4)**, 2350084.

[13] R Laxminarayan, A Duse, C Wattal, AKM Zaidi, HFL Wertheim, N Sumpradit, E Vlieghe, GL Hara, IM Gould, H Goossens, C Greko, AD So, M Bigdeli, G Tomson, W Woodhouse, E Ombaka, AQ Peralta, FN Qamar, F Mir, S Kariuki, …, O Cars. Antibiotic resistance - the need for global solutions. *The Lancet Infectious Diseases* 2013; **13(12)**, 1057-1098.

[14] AK Hassan, H Hamidinezhad and E Al-Bermany. Antibacterial activity and optical behavior for restoration of micro and nano dental fillers using functional graphene nanosheets with polymethyl methacrylate. *Nano Biomedicine and Engineering* 2024; **16(4)**, 652-664.

[15] R Vasallo-Antonio, J Peña-Bahamonde, MD Susman, JFC Ballesteros and DF Rodrigues. Design and performance of Fe_3O_4@SiO_2/MoO_3/polydopamine-graphene oxide composites for visible light photocatalysis. *Emergent Materials* 2021; **4**, 1425-1439.

[16] SS Aljelawy, E Al-Bermany and AR Abdulridha. Performance of graphene-functionalized nano chitosan in ternary polymeric nanocomposites for physical and biological applications. *Journal of Polymer Research* 2024; **31**, 226.

[17] RM Ahmed and E Al-Bermany. Innovative hydrogel MC/GO-Fe_3O_4 nanocomposites: Unveiling morphology and directorial behavior for optoelectronic device and antibacterial activity. *Emergent Materials* 2024. https://doi.org/10.1007/s42247-024-00849-0

[18] S Tan, X Wu, Y Xing, S Lilak, M Wu and JX Zhao. Enhanced synergetic antibacterial activity by a reduce graphene oxide/Ag nanocomposite through the photothermal effect. *Colloids and Surfaces B: Biointerfaces* 2020; **185**, 110616.

[19] AI Alawi and E Al-Bermany. Newly fabricated ternary PAAm-PVA-PVP blend polymer doped by SiO_2: Absorption and dielectric characteristics for solar cell applications and antibacterial activity. *Silicon* 2023; **15**, 5773-5789.

[20] HN Abdelhamid and KH Hussein. Graphene oxide as a carrier for drug delivery of methotrexate. *Biointerface Research in Applied Chemistry* 2021; **11(6)**, 14726-14735.

[21] E Al-Bermany and B Chen. Effect of the functional groups of polymers on their adsorption behavior on graphene oxide nanosheets. *Macromolecular Chemistry and Physics* 2023; **224(16)**, 2300101.

[22] CI Idumah. Design, development, and drug delivery applications of graphene polymeric nanocomposites and bionanocomposites. *Emergent Materials* 2023; **6**, 777-807.

[23] RA Abdul-Nabi and E Al-Bermany. Performers of Si_3N_4 concentrations on morphology and electrical behavior for new quinary fabrication PEO-CMC-PANI/GO@Si_3N_4 nanocomposites for electronic devise and gas sensor application. *Silicon* 2024; **16(15)**, 5583-5601.

[24] Z Huang, H Zhou, F Yuan, J Wu, S Yuan, K Cai, X Tao, X Zhang, C Tang and J Chen. Investigation on the osteogenic and antibacterial properties of silicon nitride-coated titanium dental implants. *ACS Biomaterials Science and Engineering* 2024; **10(6)**, 4059-4072.

[25] Z Xu, H Wu, F Wang, R Kaewmanee, Y Pan, D Wang, P Qu, Z Wang, G Hu, J Zhao, R Zhaod and J Wei. A hierarchical nanostructural coating of amorphous silicon nitride on polyetheretherketone with antibacterial activity and promoting responses of rBMSCs for orthopedic applications. *Journal of Materials Chemistry B* 2019; **7**, 6035-6047.

[26] M Hičák, L Medvecký, M Hnatko, R Stulajterová, M Giretová, M Tatarková, Z Lenčéš and P Šajgalík. Porous silicon nitride-based drug delivery carrier. *International Journal of Applied Ceramic Technology* 2022; **19(2)**, 882-892.

[27] P Ma, CY Yang, C Li, P Hu, F Yang, J Lu, YY Huang, H Wu, Q Wu, Y Pan and X Wang. Blow-spun Si_3N_4-incorporated nanofibrous dressing with antibacterial, anti-inflammatory, and

angiogenic activities for chronic wound treatment. *Advanced Fiber Materials* 2024; **6**, 543-560.

[28] FS Hashim, SA Jabbar, E Al-Bermany and K Abdali. Effect of inclusion ZnO-Co_3O_4 nanoparticles on the microstructural and optical properties of PVA-CMC polymeric blend for biomedical, UV shielding, and nuclear radiation shielding applications. *Plasmonics* 2024. https://doi.org/10.1007/s11468-024-02379-1

[29] E Al-Bermany and B Chen. Preparation and characterisation of poly(ethylene glycol)-adsorbed graphene oxide nanosheets. *Polymer International* 2021; **70(3)**, 341-351.

[30] MA Morsi, AH Oraby, AG Elshahawy and RMA El-Hady. Preparation, structural analysis, morphological investigation and electrical properties of gold nanoparticles filled polyvinyl alcohol/carboxymethyl cellulose blend. *Journal of Materials Research and Technology* 2019; **8(6)**, 5996-6010.

[31] SJ Pomfret, PN Adams, NP Comfort and AP Monkman. Inherently electrically conductive fibers wet spun from a sulfonic acid-doped polyaniline solution. *Advanced Materials* 1998; **10(16)**, 1351-1353.

[32] AK Al-shammari and E Al-Bermany. New fabricated (PAA-PVA/GO) and (PAAm-PVA/GO) nanocomposites: Functional groups and graphene nanosheets effect on the morphology and mechanical properties. *Journal of Physics: Conference Series* 2021; **1973(1)**, 12165.

[33] J Huang, Z Huang, S Yi, Y Liu, M Fang and S Zhang. Fe-catalyzed growth of one-dimensional α-Si_3N_4 nanostructures and their cathodoluminescence properties. *Scientific Reports* 2013; **3**, 3504.

[34] NHE Fewaty, AME Sayed and RS Hafez. Synthesis, structural and optical properties of tin oxide nanoparticles and its CMC/PEG-PVA nanocomposite films. *Polymer Science Series A* 2016; **58**, 1004-1016.

[35] EM Abdelrazek, IS Elashmawi, A El-khodary and A Yassin. Structural, optical, thermal and electrical studies on PVA/PVP blends filled with lithium bromide. *Current Applied Physics* 2010; **10(2)**, 607-613.

[36] G Cao, Q Zhang and CJ Brinker. *Annual review of nano research: Volume 3*. World Scientific, New Jersey, 2009.

[37] M Qiu, Y Zhang and B Wen. Facile synthesis of polyaniline nanostructures with effective electromagnetic interference shielding performance. *Journal of Materials Science: Materials in Electronics* 2018; **29**, 10437-10444.

[38] E Al-Bermany, AT Mekhalif, HA Banimuslem, K Abdali and MM Sabri. Effect of green synthesis bimetallic Ag@SiO_2 core-shell nanoparticles on absorption behavior and electrical properties of PVA-PEO nanocomposites for optoelectronic applications. *Silicon* 2023; **15(9)**, 4095-4107.

[39] SP Deshmukh, AG Dhodamani, SM Patil, SB Mullani, KV More and SD Delekar. Interfacially interactive ternary silver-supported polyaniline/multiwalled carbon nanotube nanocomposites for catalytic and antibacterial activity. *ACS Omega* 2020; **5(1)**, 219-227.

[40] I Moussa, R Khiari, A Moussa, MN Belgacem and MF Mhenni. Preparation and characterization of carboxymethyl cellulose with a high degree of substitution from agricultural wastes. *Fibers and Polymers* 2019; **20**, 933-943.

[41] S Khasim. Polyaniline-Graphene nanoplatelet composite films with improved conductivity for high performance X-band microwave shielding applications. *Results in Physics* 2019; **12**, 1073-1081.

[42] S Khurana and A Chandra. Ionic liquid-based organic-inorganic hybrid electrolytes: Impact of in situ obtained and dispersed silica. *Journal of Polymer Science Part B: Polymer Physics* 2018; **56(3)**, 207-218.

[43] KR Sebogodi, K Kotlhao and MJ Klink. Synthesis and characterization of graphene/polyaniline nanocomposite using green solvents. *Asian Journal of Chemistry* 2017; **29(6)**, 1206-1214.

[44] J Miao, H Li, H Qiu, X Wu and J Yang. Graphene/PANI hybrid film with enhanced thermal conductivity by in situ polymerization. *Journal of Materials Science* 2018; **53**, 8855-8865.

[45] IS Elashmawi and LH Gaabour. Raman, morphology and electrical behavior of nanocomposites based on PEO/PVDF with multi-walled carbon nanotubes. *Results in Physics* 2015;

5, 105-110.

[46] Y Liu, Y Zhu, B Mu, Y Wang, Z Quan and A Wang. Synthesis, characterization, and swelling behaviors of sodium carboxymethyl cellulose-g-poly(acrylic acid)/semi-coke superabsorbent. *Polymer Bulletin* 2022; **79(2)**, 935-953.

[47] AJ Nagajothi, R Kannan and S Rajashabala. Preparation and characterization of PEO-based composite gel-polymer electrolytes complexed with lithium trifluoro methane sulfonate. *Materials Science-Poland* 2018; **36(2)**, 185-192.

[48] J Ning, X Luo, F Wang, S Huang, J Wang, D Liu, D Chen, J Wei and Y Liu. Synergetic sensing effect of sodium carboxymethyl cellulose and bismuth on cadmium detection by differential pulse anodic stripping voltammetry. *Sensors* 2019; **19(24)**, 5482.

[49] NA Sridevi, K Karuppasamy, S Balakumar and XS Shajan. Structural and ionic conductivity studies on nanochitosan incorporated polymer electrolytes for rechargeable magnesium batteries. *Chemical Science Transactions* 2012; **1(2)**, 311-316.

[50] RAK Wardhani, L Asri, M Nasir and BS Purwasasmita. Preparation of chitosan-polyethylene oxide-*Colocasia esculenta* flour nanofibers using electrospinning method. *Journal of Mechanical Engineering Science and Technology* 2019. https://doi.org/10.17977/um016v3i12019p001

[51] M Zhang, AL Zhang, Q Li, FF Li, S Wang and SX Li. Conductivity of PEO/PLA doped liquid crystal ionomer solid polymer electrolyte in mesomorphic range. *Journal of Polymers and the Environment* 2019; **27(5)**, 2369-2379.

[52] X Hu, Y Wang, L Zhang, M Xu, J Zhang and W Dong. Design of a pH-sensitive magnetic composite hydrogel based on salecan graft copolymer and Fe_3O_4@SiO_2 nanoparticles as drug carrier. *International Journal of Biological Macromolecules* 2018; **107**, 1811-1820.

[53] S Wu, J Guo, Y Wang, C Huang and Y Hu. Facile preparation of magnetic sodium alginate/carboxymethyl cellulose composite hydrogel for removal of heavy metal ions from aqueous solution. *Journal of Materials Science* 2021; **56(23)**, 13096-13107.

[54] RM Ahmed and E Al-Bermany. Tuning the optical absorption and band gab of hydrogel methylcellulose loaded using hybrid Fe_3O_4@GO nanomaterials for optoelectronic and antibacterial activity. *Journal of Optics* 2024. https://doi.org/10.1007/s12596-024-02204-2

[55] NR Aldulaimi and E Al-Bermany. Tuning the bandgap and absorption behaviour of the newly-fabricated ultrahigh molecular weight polyethylene oxide-polyvinyl alcohol/graphene oxide hybrid nanocomposites. *Polymers and Polymer Composites* 2022. https://doi.org/10.1177/09673911221112196

[56] N Tohluebaji, R Siri, N Muensit, C Putson, P Channuie, P Porrawatkul and J Yuennan. Hydrophobic and optical properties of P(VDF-HFP) nanofiber filled with nickel (II) chloride hexahydrate for dye-sensitized solar cells application. *Trends in Sciences* 2024; **21(9)**, 8762.

[57] E Maslova, L Eisaiankhongi, F Sjöberg and RR McCarthy. Burns and biofilms: Priority pathogens and *in vivo* models. *NPJ Biofilms and Microbiomes* 2021; **7(1)**, 73.

[58] D McDougald, SA Rice, N Barraud, PD Steinberg and S Kjelleberg. Should we stay or should we go: Mechanisms and ecological consequences for biofilm dispersal. *Nature Reviews Microbiology* 2012; **10(1)**, 39-50.

[59] IA Ibrahim, RM Al-Shwaikh and MI Ismaeil. Virulence and antimicrobial resistance of *Escherichia coli* isolated from Tigris River and children diarrhea. *Infection and Drug Resistance* 2014; **7**, 317-322.

[60] ZHA Al-Saadi and RM Abdullah. Phenotypic and molecular detection of *Escherichia coli* efflux pumps from UTI patients. *Biochemical and Cellular Archives* 2019; **19(S1)**, 2371-2376.

[61] P Negi, J Chadha, K Harjai, VS Gondil, S Kumari and K Raj. Antimicrobial and antibiofilm potential of green-synthesized graphene-silver nanocomposite against multidrug-resistant nosocomial pathogens. *Biomedicines* 2024; **12(5)**, 1104.

[62] MD Giulio, R Zappacosta, SD Lodovico, ED Campli, G Siani, A Fontana and L Cellini. Antimicrobial and antibiofilm efficacy of graphene oxide against chronic wound

microorganisms. *Antimicrobial Agents and Chemotherapy* 2018; **62(7)**, e00547-18.

[63] KH Tay, LHB Sim and SK Chidambaram. Efficacy of baricitinib in patients treated with corticosteroids for severe Covid-19 pneumonia: A retrospective observational cohort study. *International Journal of Infectious Diseases* 2023; **130(S2)**, S96.

[64] H Zhou, C Persson, O Donzel-Gargand, H Engqvist and W Xia. Structural Si_3N_4-SiO_2 glass ceramics with bioactive and anti-bacterial properties. *Journal of the European Ceramic Society* 2024; **44(6)**, 4260-42671.